Journal of Advanced Ceramics
2022, **11**(6): 961–973
https://doi.org/10.1007/s40145-022-0589-z
ISSN 2226-4108
CN 10-1154/TQ

Research Article

High-entropy rare-earth zirconate ceramics with low thermal conductivity for advanced thermal-barrier coatings

Debao LIU[a], Baolu SHI[a], Liyan GENG[b], Yiguang WANG[a], Baosheng XU[a,*], Yanfei CHEN[a]

[a]*Institute of Advanced Structure Technology*, *Beijing Institute of Technology*, *Beijing 100081*, *China*
[b]*Shanghai Space Propulsion Technology Research Institute*, *Shanghai 201109*, *China*

Received: November 21, 2021; Revised: March 16, 2022; Accepted: March 19, 2022

Abstract: The high-entropy rare-earth zirconate ($(La_{0.2}Nd_{0.2}Sm_{0.2}Gd_{0.2}Yb_{0.2})_2Zr_2O_7$, $5RE_2Zr_2O_7$ HE-REZs) ceramics were successfully prepared by a new high-speed positive grinding strategy combined with solid-state reaction method. The microstructure, crystal structure, phase composition, and thermophysical and mechanical properties of the samples were systematically investigated through various methods. Results indicate that the samples have a single-phase defect fluorite-type crystal structure with excellent high-temperature thermal stability. The as-prepared samples also demonstrate low thermal conductivity (0.9–1.72 $W \cdot m^{-1} \cdot K^{-1}$ at 273–1273 K) and high coefficient of thermal expansion (CTE, 10.9×10^{-6} K^{-1} at 1273 K), as well as outstanding mechanical properties including large Young's modulus (E = 186–257 GPa) and high fracture toughness (K_{IC}). Furthermore, the formation possibility of the as-prepared samples was verified through the first-principles calculations, which suggested the feasibility to form the $5RE_2Zr_2O_7$ HE-REZs in the thermodynamic direction. Therefore, in view of the excellent multifunctional properties exhibited by the as-prepared $5RE_2Zr_2O_7$ HE-REZs, they have great potential applications in next-generation thermal-barrier coatings (TBCs).

Keywords: high-entropy rare-earth zirconates (HE-REZs); first-principles calculations; thermal conductivity; thermal stability; Young's modulus; thermal-barrier coatings (TBCs)

1 Introduction

Thermal-barrier coatings (TBCs), as refractory ceramic materials, are extensively used in aircraft engines and industrial gas turbines to protect their metallic components against high temperatures during operation, which can extend the lifespan of metallic components and energy efficiency at elevated operation temperatures [1–4]. Generally, the state-of-the-art TBCs have some important merits, such as high melting point, low thermal conductivity, favorable chemical stability, ideal sintering resistance with no phase transformation at elevated temperature, enhanced mechanical properties, and matched coefficients of thermal expansion (CTEs) with the metallic substrate [5,6]. Over the past decades, TBCs have undergone considerable development to satisfy the growing demand for high operating temperatures. Some representative TBCs such as 6–8 wt% Y_2O_3-stabilised ZrO_2 (YSZ) [7], $Yb_3Al_5O_{12}$ [8], and mullite [9] have been extensively studied. Amongst

* Corresponding author.
E-mail: xubsh@bit.edu.cn

these materials, YSZ has captured research interest and become a typical TBC owing to its low thermal conductivity, relatively high fracture toughness (K_{IC}), and high CTEs [7]. Unfortunately, the formation of the cubic and tetragonal phase of YSZ results in volumetric expansion and spallation when the working operation temperature exceeds 1473 K, which leads to the failure of YSZ TBCs. Additionally, the poor sintering resistance of YSZ at elevated temperatures could lead to increasing the thermal conductivity. Therefore, the production of new-generation TBCs with long-term serviceability at high temperature is desirable.

Great efforts have been exerted to investigate several kinds of new promising TBC candidates at high operation temperatures, such as $RE_2Zr_2O_7$ (rare-earth zirconates; RE, rare-earth element) [10], $REPO_4$ [11], and $RE_2Al_4O_9$ [12]. Amongst these new candidates, pyrochlore-type or fluorite-type structured $RE_2Zr_2O_7$ exhibit excellent performance, including low thermal conductivity, high CTE value, high phase stability, and low oxygen-ion diffusivity than those of YSZ [13,14], making them very important promising TBCs. The crystal structure of $RE_2Zr_2O_7$ depends on the ionic radius ratio of the RE atom and the Zr atom (R_{RE}/R_{Zr}). When the R_{RE}/R_{Zr} value ranges within 1.46–1.78, $RE_2Zr_2O_7$ presents a pyrochlore-type structure; when R_{RE}/R_{Zr} value is less than 1.46, $RE_2Zr_2O_7$ acquires the defective-type fluorite structure [15]. As reported in Ref. [16], the 4f orbital of RE atoms in $RE_2Zr_2O_7$ plays an important role in chemical-bond formation. The bond length is shortened by mixing the RE atoms with its matches, so the crystal binding energy of the materials accordingly increases, demonstrating apparent influence on the thermophysical and mechanical properties of $RE_2Zr_2O_7$ TBCs. However, the developed $RE_2Zr_2O_7$ TBCs usually exhibit poor durability, and their CTEs should be further enhanced to meet the requirement for application as advanced next-generation TBCs [17].

High-entropy ceramics (HECs), as a single-phase solid solution with multiprincipal elements, have attracted increased attention because of some intriguing properties. These properties include low thermal conductivity, excellent mechanical properties, and improved chemical stability and oxidation resistance compared with those of their single-component counterparts [18–20]. The overall performance of HECs can reportedly be affected by four aspects, namely, severe lattice distortion, high entropy, sluggish diffusion, and cocktail effects [21,22]. Inspired by the HEC concept, $RE_2Zr_2O_7$ HECs have been investigated by doping methods with more kinds of RE elements. For example, Zhao *et al.* [23] fabricated $(La_{0.2}Ce_{0.2}Nd_{0.2}Sm_{0.2}Eu_{0.2})_2Zr_2O_7$ HECs, which exhibit sluggish grain growth and an ultra-low thermal conductivity of 0.76 $W\cdot m^{-1}\cdot K^{-1}$ at room temperature. Ren *et al.* [13] prepared $(Sm_{0.2}Eu_{0.2}Tb_{0.2}Dy_{0.2}Lu_{0.2})_2Zr_2O_7$ HECs with defective fluorite structure, showing a considerably lower thermal conductivity of 0.86 $W\cdot m^{-1}\cdot K^{-1}$ at 1273 K than its counterparts. Zhou *et al.* [24] synthesized $(La_{0.2}Nd_{0.2}Sm_{0.2}Eu_{0.2}Gd_{0.2})_2Zr_2O_7$ HECs through solid-phase reaction method. They exhibited excellent thermal stability and improved thermal shock resistance properties owing to the sluggish diffusion effect and well matched CTEs with its base parts. Li *et al.* [25] produced pyrochlore-type $(5RE_{1/5})_2Zr_2O_7$, which demonstrates low thermal conductivity below 1 $W\cdot m^{-1}\cdot K^{-1}$ (573–1473 K), high sintering resistance, and excellent thermal stability. The present research primarily focused on several properties of $RE_2Zr_2O_7$ HECs prepared by traditional solid-state reaction method (including the time-consuming ball-milling process), rather than taking a research in many ways, such as theoretical calculations and multifunctional properties. The particle size of the reported $RE_2Zr_2O_7$ HECs was on the micron scale. Thus, special attention should be paid to the preparation of $RE_2Zr_2O_7$ HECs with an efficient solution and the analysis of the overall criterion based on the theoretical calculations and experimentally measured properties.

Herein, we synthesized novel $(La_{0.2}Nd_{0.2}Sm_{0.2}Gd_{0.2}Yb_{0.2})_2Zr_2O_7$ ($5RE_2Zr_2O_7$) HECs by using a new high-speed grinding strategy combined with a solid-state reaction method. The microstructure, phase composition, theoretical calculation, and thermophysical and mechanical properties of the samples were systematically investigated. The standard for selecting the five RE elements was based on the large difference in ion radius that easily formed the defective fluorite-type structure, which can enhance the "high-entropy effect" owing to numerous O vacancies and disordered distributions, thereby improving the thermophysical or mechanical properties of the HE-REZs. Notably, the traditional preparation method uses the passive planetary ball-milling process, which requires a long time (24 h), and the particle size of the powders is in the micron range. However, in the current work, we adopted the advanced high-speed positive grinding process with a maximum speed of up to 700 $r\cdot min^{-1}$, demonstrating a short time (3 h). The particle size of the obtained

powders was close to the micron or nanometer level. In the aspect of structural characterization, we introduced the Raman spectroscopy and FT-IR spectroscopy to verify the type of chemical bond between atoms and crystal structure of the samples. The two techniques are rarely mentioned in the previous related works. Moreover, the first-principles calculations based on density functional theory (DFT) was used to prove the possible formation of the $5RE_2Zr_2O_7$ HE-REZs. Specifically, it was used to verify that the mixed Gibbs free energy (ΔG_{mix}) decreased with increased temperature (T) under the condition of high entropy, indicating the feasibility to form $5RE_2Zr_2O_7$ HE-REZs in the thermodynamic direction. To the best of our knowledge, the potential application value of HE-REZs in TBCs has been characterized from these three aspects of theoretical calculations, thermophysical properties, and mechanical properties. This work points out a novel strategy and offers great value for the design of advanced next-generation TBCs with excellent multifunctional properties.

2 Experimental and calculation procedures

2. 1 Materials

Commercially available La_2O_3, Nd_2O_3, Sm_2O_3, Gd_2O_3, and Yb_2O_3 (particle size D_{50} = 5 μm, purity ⩾ 99.99%) were purchased from Shanghai Diyang Co., Ltd., Shanghai, China. Monoclinic ZrO_2 (particle size D_{50} = 0.2 μm, purity ⩾ 99.99%) was purchased from Sinopharm Chemical Reagent Co., Ltd., Shanghai, China. The above reagents served as starting materials and were used as received.

2. 2 Preparation of samples

The raw materials were stoichiometrically weighed and ball milled (ZrO_2 ball, ϕ = 2 mm) using a vertical mixing ball-milling equipment (Union Process, 01-HD, USA) with ethanol as the medium for 3 h at 600 $r \cdot min^{-1}$. The mixed powders were dried at 363 K for 24 h and sifted through a 200-mesh sieve before granulation and then through an 80-mesh sieve. Afterwards, the ground powder mixtures were condensed into sheets (ϕ = 30 mm) at a uniaxial pressure of 25 MPa for 3 min and then cold isostatic pressed under 200 MPa for 2 min. The obtained pressed disks were calcined at 873 K for 3 h (1 ℃·min^{-1}) to burn out the polyvinyl acetate (PVA) binders and then at 1773 K for 3 h (2 ℃·min^{-1}) in the air for densification. For comparison, the reference single RE zirconate $RE_2Zr_2O_7$ ($La_2Zr_2O_7$ or $Yb_2Zr_2O_7$) ceramics and medium-entropy RE zirconate $3RE_2Zr_2O_7$ ($(La_{1/3}Sm_{1/3}Yb_{1/3})_2Zr_2O_7$) ceramics were also prepared under the same conditions.

2. 3 Structure characterisation methods

The field-emission scanning electron microscope (SEM; FEI Quanta 600) equipped with energy-dispersive spectroscope (EDS; Oxford INCAxsight 6427) was applied to observe the morphology and elemental distributions of the samples. The transmission electron microscope (TEM; JEOL 2010 F, Japan) with selected-area electron diffraction (SAED) analysis was used to examine the morphological characteristics and crystalline structure of the obtained samples. The phases of the samples were characterized by the X-ray diffractometer (Bruker D8 Advance). Theoretical density (ρ_0) and experimental density (ρ) were measured based on the lattice parameter measured by the X-ray diffraction (XRD) patterns and the Archimedes method, respectively. Thermogravimetric analysis (TGA) and differential scanning calorimetry (DSC) were performed using a thermogravimetric analyser (NETZSCH STA 449F3, Germany). Raman spectra were obtained on a microscopic confocal Raman spectrometer (Renishaw, RM2000, UK) by using an argon-ion laser with radiation at 532 nm. The Fourier transform infrared (FT-IR) spectra were recorded on a WQF-410 spectrophotometer (Beijing Secondary Optical Instruments, China).

2. 4 First-principles calculations

We used the Vienna *ab initio* simulation package by using the Cambridge serial total energy package (CASTEP) code to perform the first-principles calculations based on DFT [26]. Through the first-principles calculations, the stoichiometry and mobility of RE, Zr, and O atoms in $5RE_2Zr_2O_7$ were verified. The mixing enthalpy (H_{mix}) was calculated from a 5 × 1 × 1 supercell with $La_4Nd_4Sm_4Gd_4Yb_4Zr_{20}O_{70}$. The generalized gradient approximation of Perdew–Burke–Ernzerhof was used to characterize the exchange-correlation energy [27]. Under the condition of integrated Brillouin zone, the k-point mesh was divided into 2 × 1 × 2 using the Monkhorst–Pack method.

ΔH_{mix} was defined as the energy relative to five single RE zirconates, according to Eq. (1):

$$\Delta H_{\text{mix}}(La_4Nd_4Sm_4Gd_4Yb_4Zr_{20}O_{70}) = \frac{E_{\text{total}}(La_4Nd_4Sm_4Gd_4Yb_4Zr_{20}O_{70}) - E_{\text{total}}(RE_8Zr_8O_{28})}{110} \quad (1)$$

where $E_{\text{total}}(La_4Nd_4Sm_4Gd_4Yb_4Zr_{20}O_{70})$ and $E_{\text{total}}(RE_8Zr_8O_{28})$ are the total energy of high-entropy $RE_2Zr_2O_7$ and the total energy of single $RE_2Zr_2O_7$, respectively.

Given the equal relationship of the RE elements, the ideal mixed entropy (S_{mix}) of the supercell $La_4Nd_4Sm_4Gd_4Yb_4Zr_{20}O_{70}$ was calculated to be as Eq. (2) [28]:

$$S_{\text{mix}} = R \ln N \quad (2)$$

where R is the ideal gas constant (8.314 $J \cdot mol^{-1} \cdot K^{-1}$), and N is the number of microstates. Thus, the mixed Gibbs free energy (G_{mix}) can be calculated as Eq. (3) [29]:

$$G_{\text{mix}} = H_{\text{mix}} - TS_{\text{mix}} \quad (3)$$

Obviously, G_{mix} can be reduced (the $5RE_2Zr_2O_7$ system stabilized) by reducing the H_{mix} values or increasing the TS_{mix} values.

2.5 Thermophysical property measurement

The thermal conductivity (κ) of the samples was calculated from the thermal diffusivity (λ), specific heat capacity (c_p), and ρ:

$$\kappa = \lambda \cdot \rho \cdot c_p \quad (4)$$

We determined λ by laser-reflection method (NETZSCH, LFA-457, Germany) from ambient temperature to 1273 K and calculated c_p based on the Neumann–Kopp law [30].

The CTEs of the samples (3 mm × 3 mm × 10 mm) were measured using a high-temperature dilatometer analyzer (TMA 402 F3, Germany). The as-prepared $5RE_2Zr_2O_7$ ceramic bulks were heat treated at 1573 K for 5–40 h to evaluate their thermal stability at high temperature.

2.6 Mechanical performance analysis

The Vickers hardness (HV) of the samples was measured under the force of 0.5 kgf with a holding time of 10 s using a Vickers hardness tester (Shanghai Yanrun Optoelectronics Technology Co., Ltd., HV-50Z, China). The Young's modulus (E) was tested using a nanoindenter (Indenter G200). Each specimen was measured three times, and the average value was taken for accuracy. The value of HV was calculated as Eq. (5) [13]:

$$\text{HV} = 0.1891\frac{F}{d^2} \quad (5)$$

where F and d are the indentation load and indent diagonal length, respectively. Thus, K_{IC} can be obtained based on HV and E [31]:

$$K_{\text{IC}} = 0.016\left(\frac{E}{\text{HV}}\right)^{1/2}\frac{F}{C^{3/2}} \quad (6)$$

where C (half-length of the crack) is the distance from the center of indentation to the tip of the crack.

3 Results and discussion

3.1 Phase stability and structural characterization

Figure 1 demonstrates the crystal structures of pyrochlore-type and defective fluorite-type structures. The ideal pyrochlore-type structure (Fig. 1(a)) belongs to the space group $Fd\bar{3}m$ (Z = 8). In this kind of structure, the zirconium atoms equally occupy the 16d site, whereas RE atoms homogeneously occupy the 16c site. Specifically, the oxygen atoms occupy the 8b and 48f sites, whereas the oxygen vacancy occupies the 8a site [32,33]. Meanwhile, the defective fluorite-type structure (Fig. 1(b)) exhibits the space group of $Fm\bar{3}m$ (Z = 1).

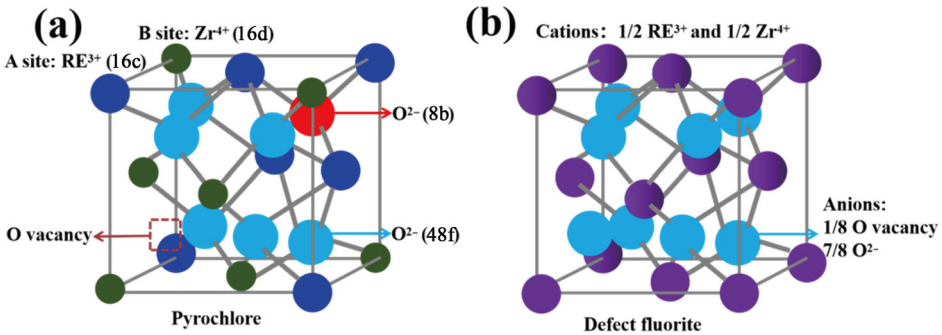

Fig. 1 Schematic of crystal structure of pyrochlore and defective fluorite: (a) 1/8 of unit cell of pyrochlore structure and (b) defective fluorite structure.

In this kind of structure, the cations and oxygen vacancies all demonstrate disordered distribution states [34].

The SEM images with corresponding elemental mappings of the as-prepared powders are shown in Fig. 2. The EDS elemental mapping results revealed that the RE, zirconium, and oxygen elements were uniformly distributed throughout the entire field, indicating that all samples were chemically homogeneous.

Figure 3(a) shows the microstructure of $5RE_2Zr_2O_7$ ceramic bulk, which presented no obvious microvoids

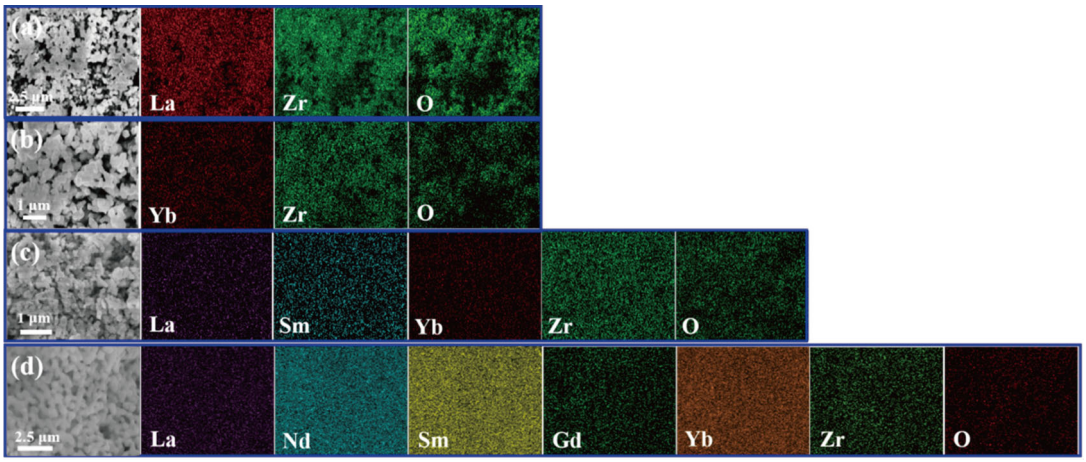

Fig. 2 SEM images and elemental mappings for (a) $La_2Zr_2O_7$, (b) $Yb_2Zr_2O_7$, (c) $3RE_2Zr_2O_7$, and (d) $5RE_2Zr_2O_7$ powders.

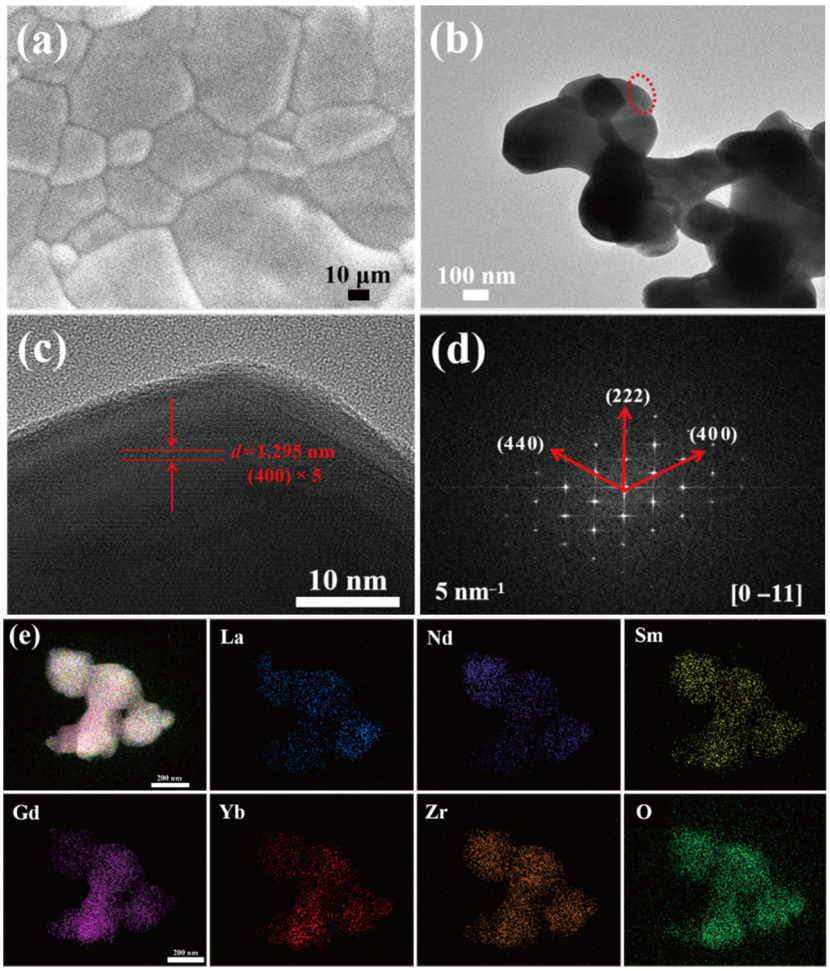

Fig. 3 (a) Microstructure of sintered $5RE_2Zr_2O_7$ ceramic bulk; (b) TEM image, (c) HRTEM image, (d) SAED pattern, and (e) TEM–EDS elemental mappings of $5RE_2Zr_2O_7$ ceramic powders.

on the polished and thermally etched surface. To further verify the elemental distribution and structure information, TEM and high resolution TEM (HRTEM) technology were used. As depicted in Fig. 3(b), irregular particles (about 210 nm) of the microscale agglomerated together to form micronized particles. The HRTEM (Fig. 3(c)) image shows a lattice spacing of 0.259 nm, corresponding with the (400) plane [35], and the lattice parameter (d_{hkl}) was calculated to be 10.631 Å (based on Eq. (7)). The lattice parameters calculated from the XRD patterns and densities of the samples are shown in Table 1. The relative densities (ρ_r) of the samples ranged between 98.47% and 98.89%.

$$d_{hkl} = \frac{a}{\sqrt{h^2 + k^2 + l^2}} \tag{7}$$

The SAED pattern along the [0−11] zone axis (Fig. 3(d)) also reveals that $5RE_2Zr_2O_7$ had a single defective fluorite structure. All elements (La, Nd, Sm, Gd, Yb, Zr, and O), as shown in Fig. 3(e), were homogeneously distributed on the microscale without noticeable elemental segregation or clustering.

Figure 4(a) shows the XRD patterns of the as-prepared $5RE_2Zr_2O_7$ ceramic powders. No characteristic reflections of impurities were detected, demonstrating a pure face-centered cubic defective fluorite structure. Specifically,

Table 1 Calculated lattice parameters and ρ, ρ_0, and ρ_r of the ceramics after sintering at 1573 K for 3 h

Sample	Lattice parameter (Å)	ρ (g·cm^{-3})	ρ_0 (g·cm^{-3})	ρ_r (%)
$La_2Zr_2O_7$	10.810	7.13	7.23	98.62
$Yb_2Zr_2O_7$	10.764	7.14	7.24	98.61
$3RE_2Zr_2O_7$	10.642	7.11	7.22	98.47
$5RE_2Zr_2O_7$	10.631	7.13	7.21	98.89

Note: $\rho_r = \rho/\rho_0$

the XRD pattern peaks had different degrees of shift compared with those of each pure single counterpart owing to the solid-solution effect [36]. Figure 4(b) shows the XRD patterns of the ceramic bulks. Obviously, the $5RE_2Zr_2O_7$ and $3RE_2Zr_2O_7$ ceramic bulks still obtain the characteristic diffraction peaks of the defective fluorite structure without impurities. Notably, the peaks marked with black club for the $La_2Zr_2O_7$ were characteristic superlattice diffraction peaks belonging to the pyrochlore structure [37]. The absence of weak peaks of $La_2Zr_2O_7$ may be explained by the strange defective fluorite structure of $Yb_2Zr_2O_7$, which had no supperlattice diffraction peaks.

Figures 5(a)–5(f) show the ball-and-stick models of primitive cells obtained through the first-principles calculations based on DFT. As depicted in Figs. 5(a)–5(e), single $RE_2Zr_2O_7$ (RE = La, Nd, Sm, Gd, and Yb) demonstrated the pyrochlore-type structure. Meanwhile, RE atoms equally occupied the 16c sites, and zirconium atoms were located at the 16d sites. Oxygen vacancy atoms were at the 8a site, whereas O atoms occupied the 8b and 48f sites [30]. However, the structure of $5RE_2Zr_2O_7$, as depicted in Fig. 5(f), exhibited the defective fluorite type in which RE elements and zirconium atoms were equally and randomly located at the 4a sites, whereas the oxygen vacancy atoms were randomly distributed at the 8b sites [33]. During the calculation process, the equilibrium lattice constants of $RE_2Zr_2O_7$ (RE = La, Nd, Sm, Gd, and Yb) primitive cell were optimized by using a 5 × 5 × 5 Monkhorst–Pack *k*-point grid for Brillouin zone sampling. Thus, the lattice constants ($a = b = c$, $\alpha = \beta = \gamma = 60°$) were 7.576, 7.510, 7.454, 7.401, 7.368, and 7.483 Å for $La_2Zr_2O_7$, $Nd_2Zr_2O_7$, $Sm_2Zr_2O_7$, $Gd_2Zr_2O_7$, $Yb_2Zr_2O_7$, and $RE_2Zr_2O_7$, respectively.

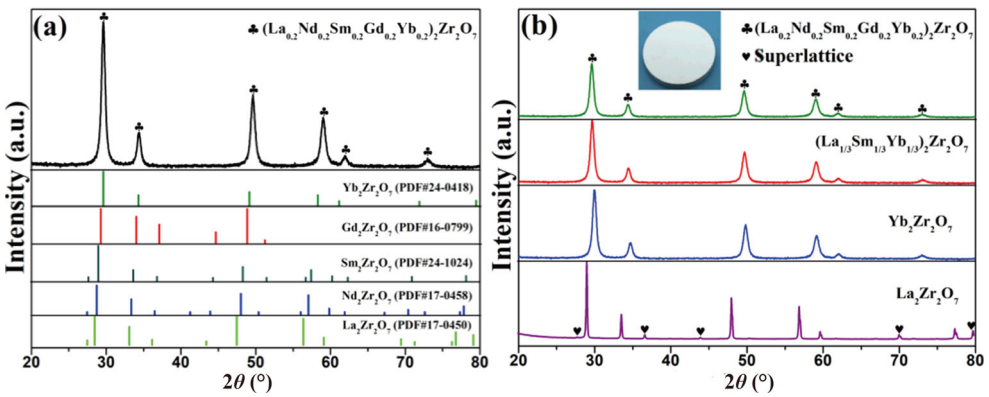

Fig. 4 XRD patterns of (a) $5RE_2Zr_2O_7$ ceramic powders and (b) $La_2Zr_2O_7$, $Yb_2Zr_2O_7$, $3RE_2Zr_2O_7$, and $5RE_2Zr_2O_7$ ceramic bulks.

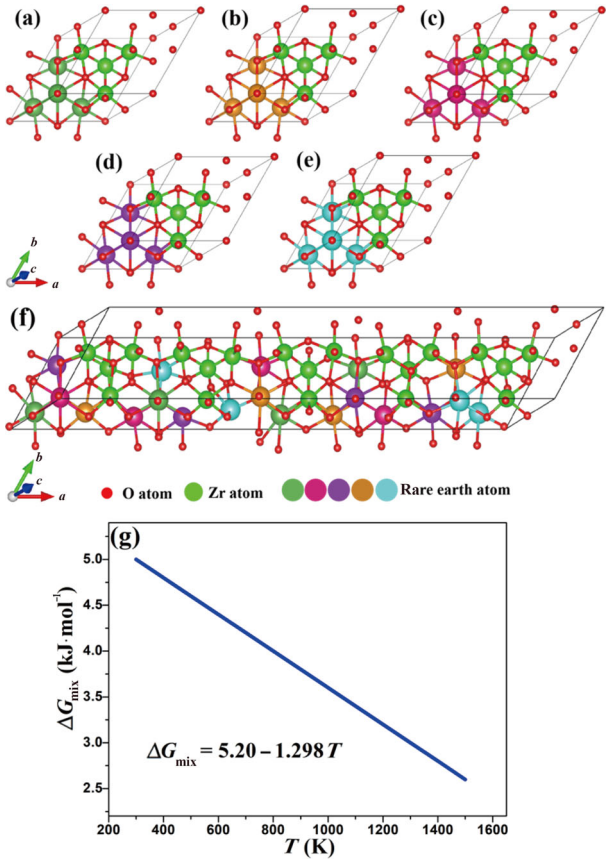

Fig. 5 Ball-and-stick models of primitive cells obtained through the first-principles calculations based on DFT. (a) $La_2Zr_2O_7$, (b) $Nd_2Zr_2O_7$, (c) $Sm_2Zr_2O_7$, (d) $Gd_2Zr_2O_7$, (e) $Yb_2Zr_2O_7$, and (f) 5 × 1 × 1 supercell for $RE_2Zr_2O_7$ (RE = La, Nd, Sm, Gd, and Yb). (g) ΔG_{mix} of $5RE_2Zr_2O_7$ at different T.

When neglecting the effect of lattice vibrational contribution, the ΔH_{mix} and ΔS_{mix} values were calculated to be 5.20 and 1.298 kJ·mol^{-1} according to Eqs. (1) and (2), respectively. Furthermore, the positive ΔH_{mix} value indicated an endothermic reaction for the formation of $5RE_2Zr_2O_7$. Therefore, the mixing Gibbs free energy (ΔG_{mix}) can be calculated according to Eq. (3). The relationship between ΔG_{mix} and T (Fig. 5(g)) indicated a possible stabilized solid solution.

Figure 6(a) presents the Raman spectra of the samples. Six Raman active vibration modes associated with an O cation were included in an ideal pyrochlore structure [38]:

$$\Gamma(\text{Raman}) = A_{1g} + E_g + 4_{2g} \quad (8)$$

However, only one vibration mode (F_{2g}) is present in an ideal fluorite structure. Obviously, $Sm_2Zr_2O_7$ ($RE_2Zr_2O_7$) had four typical vibration modes, indicating a pyrochlore structure. Furthermore, a broad and weak Raman peak can be found in the sample $3RE_2Zr_2O_7$ and only one vibration mode (F_{2g}) was observed in the sample $5RE_2Zr_2O_7$, which can be ascribed to the disordered structures from a high-entropy effect [39].

As depicted in the FT-IR spectra (Fig. 6(b)), the peaks centered at 1187 and 1108 cm^{-1} were ascribed to the stretching vibration of the Zr–O–Zr bond [40]. Meanwhile, the peaks near 540 and 3690 cm^{-1} corresponded with the vibration of the Zr–O stretching modes. A weak band centered at about 436 cm^{-1} was associated with the vibration of the O–RE–O bending modes [41]. Specifically, peaks centered at 1380–1630 cm^{-1} were due to the water molecules in the tested powders. However, no obvious characteristic peaks in the samples $3RE_2Zr_2O_7$ and $5RE_2Zr_2O_7$ were found because of the composition disorder caused by the high-entropy effect [42].

The TGA curve (Fig. 6(c)) presents a slight weight loss within a wide temperature range of 373–1473 K, which can be ascribed to the evaporation of the absorbed and bound water in the samples. The DSC curve indicated that the structure phase remained stable up to 1473 K because no significant endothermic or exothermic peaks appeared.

Generally, sintering resistance is an important

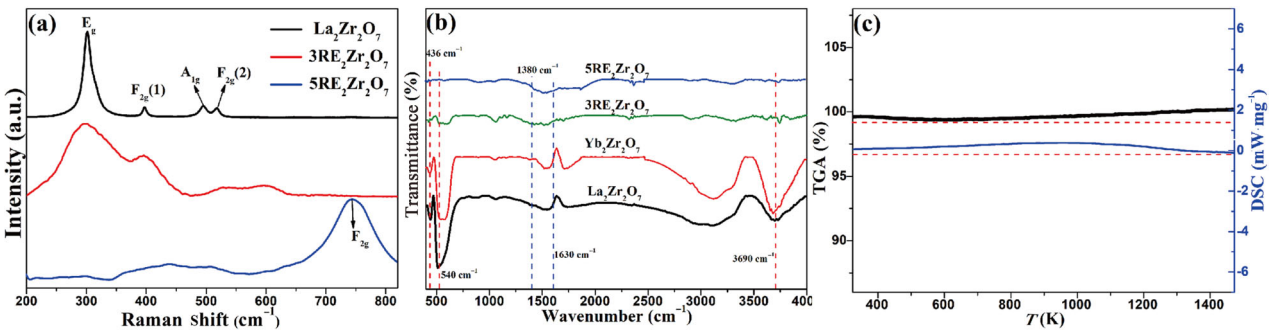

Fig. 6 Analysis of (a) Raman spectra and (b) FT-IR spectra of the samples. (c) TGA and DSC curves of the as-prepared $5RE_2Zr_2O_7$.

criterion for TBCs [43]. The $5RE_2Zr_2O_7$ samples were aged at 1573 K for different time (Figs. 7(a)–7(c)) to evaluate their high-temperature stability. The coarse grains indicated that the grain boundaries were thermally etched. Grain sizes can be calculated within the range of 300–420, 340–460, and 370–510 nm for Figs. 7(a), 7(b), and 7(c), respectively. Clearly, the average grain size did not show an apparent change, which can be ascribed to the sluggish diffusion effect [24]. The corresponding XRD patterns (Fig. 7(d)) indicate that all the samples still had the defective fluorite-type structures with no phase decomposition. Moreover, no XRD peaks shifted, and no transformation was detected. Therefore, the as-prepared $5RE_2Zr_2O_7$ exhibited excellent sintering resistance and thermal stability at high temperature.

3. 2 Thermophysical properties

As shown in Fig. 8(a), the increased c_p values with increased T can be ascribed to the volumetric expansion and phonon excitation [44]. The experimental thermal diffusivities (Fig. 8(b)) showed a decrease tendency with increased T at 273–873 K, followed by a slight increase with prolonged T duration owing to the thermal-radiation effect at high temperature [13]. The crystal structure and lattice defects (pores and oxygen vacancies) were the main reason for the decreased thermal diffusivity. The distortion of oxygen vacancies can increase the distorted oxygen sublattice according to the point-defect scattering theory [45]. The thermal-radiation effect can be neglected at a low temperature (below 873 K), and the reciprocal thermal diffusivity (α^{-1}) was proportional to T [46]:

$$\frac{1}{\alpha} \sim \frac{1}{l(w,T)} \sim \left(\frac{bn^{1/3}C}{\theta_D}\right)T + \left(D - \frac{C}{2}\right) \tag{9}$$

where $\frac{1}{l(w,T)}$ is the phonon mean free path; b, C, and D are constants; n is the number of atoms in the primitive cell; and θ_D is the Debye temperature. As shown in Fig. 8(c), α^{-1} had a linear relationship (273–873 K) that gradually decreased with prolonged T duration owing to the thermal-radiation effect. The thermal-radiation conductivity (K_r) at elevated T (above 873 K) can be expressed as follows [47]:

$$K_r = 16n^2\sigma T^3\varepsilon^{-1} \tag{10}$$

where n, σ, and ε are the mean refractive index, Stefan–Boltzmann constant, and extinction coefficient, respectively. Clearly, the thermal-radiation conductivity was directly proportional to T. Thus, the thermal conductivities of the as-prepared samples increased with increased T. The sample $5RE_2Zr_2O_7$, as shown in Fig. 8(d), had the lowest experimental thermal conductivity

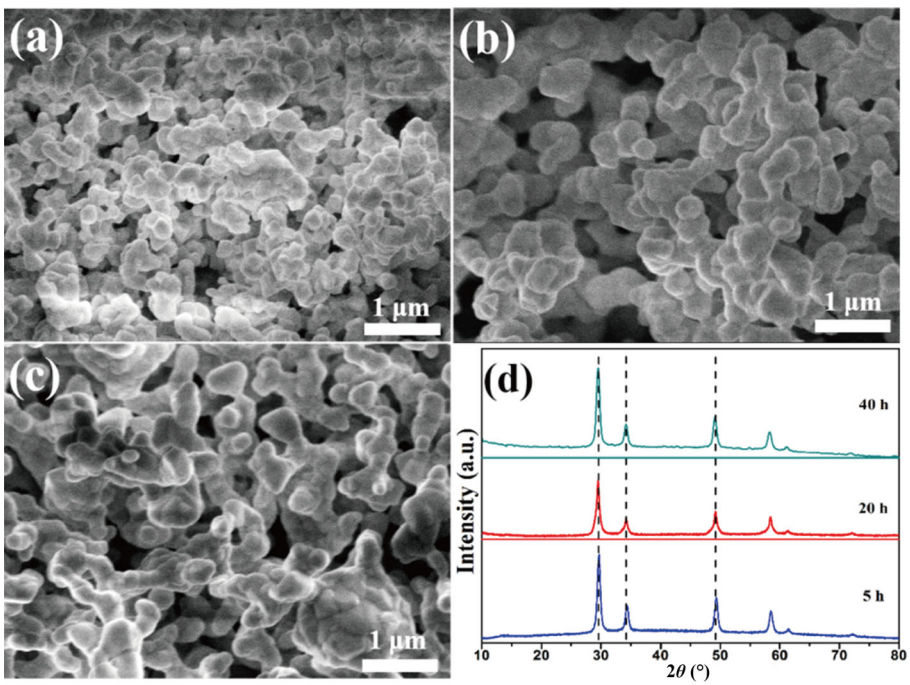

Fig. 7 SEM images of $5RE_2Zr_2O_7$ after thermal treatment at 1573 K for different time: (a) 5 h, (b) 20 h, and (c) 40 h. (d) Corresponding XRD patterns of the thermal-treated $5RE_2Zr_2O_7$.

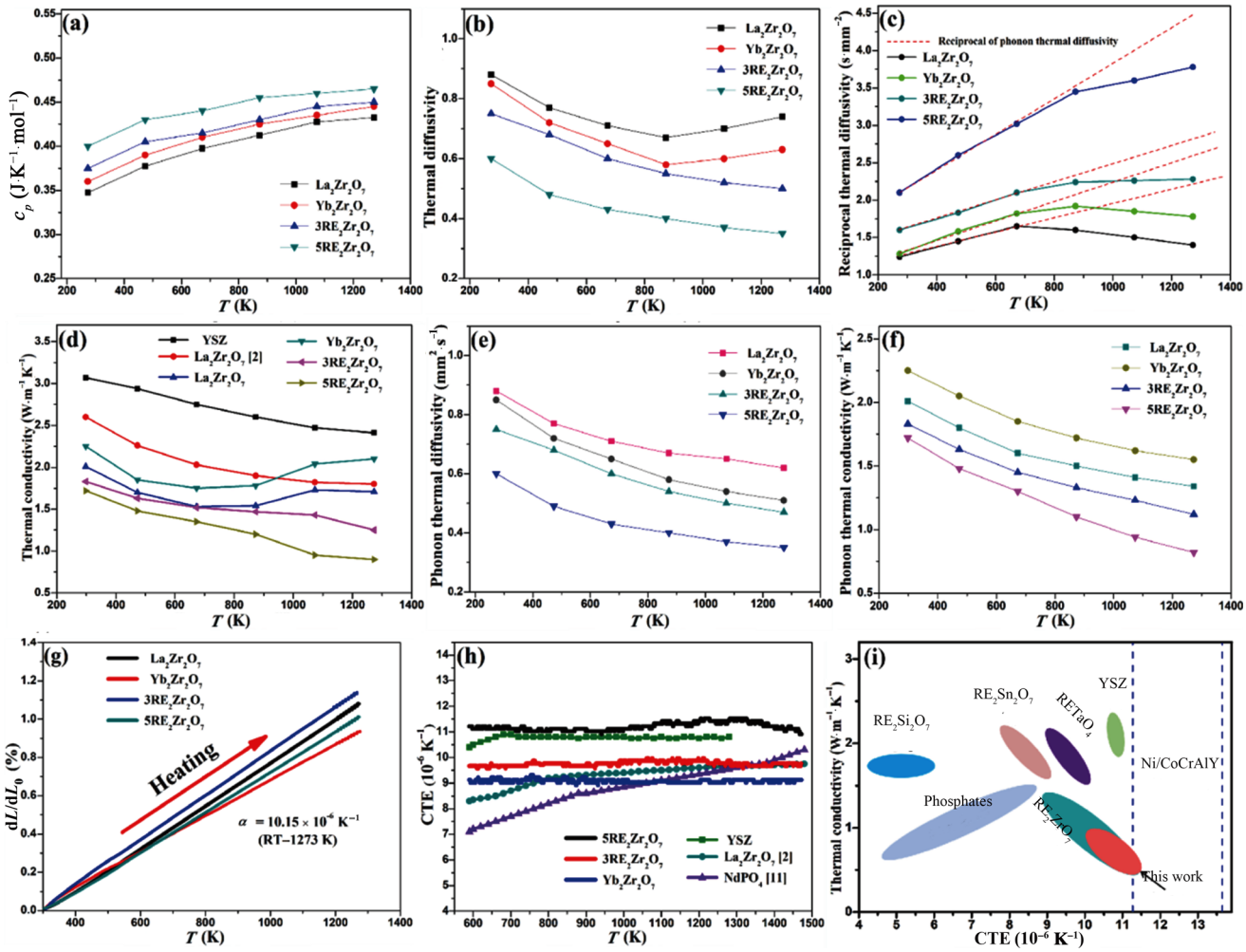

Fig. 8 Thermophysical properties of the samples: (a) c_p, (b) thermal diffusivity, (c) reciprocal of thermal diffusivity, (d) experimental thermal conductivity, (e) phonon thermal diffusivity, (f) phonon thermal conductivity, (g) linear thermal expansion curve, (h) CTE, and (i) thermal conductivity as a function of CTE.

(0.9 W·m^{-1}·K^{-1} at 1273 K) compared with those of YSZ and its counterparts within the entire temperature range. The linear relationship was fitted (273–873 K) and then extrapolated to 1273 K. The phonon thermal diffusivities and phonon thermal conductivities were then obtained, as shown in Figs. 8(e) and 8(f), respectively. The phonon–phonon scattering process can be enhanced with increased high temperature, as well as the lattice distortion and quality difference caused by the high- entropy effect, which can together decrease the mean free path and thus decrease the thermal conductivity of the samples [48].

To further explore how the defects intrinsically affected the thermal conductivity, we determined the proportional relationship between actual thermal conductivity (k) and defect-free thermal conductivity (k_p) as Eqs. (11) and (12) [49]:

$$\frac{k}{k_p} = \frac{\arctan u}{u} \tag{11}$$

$$u = \left(\frac{\pi^2 \theta_D \Omega}{h v_a^2} k_p \Gamma\right)^{1/2} \tag{12}$$

where Ω, Γ, θ_D, h, and v_a represent the average atomic volume, phonon scattering coefficient, Debye temperature, Planck's constant, and average acoustic velocity, respectively. Obviously, Γ plays a vital role in decreasing the actual thermal conductivity and can be described as Eq. (13) [50]:

$$\Gamma = f_i \left\{ \left(\frac{\Delta M_i}{M}\right)^2 + 2\left[6.4 \times \frac{1}{3}\gamma \frac{1+\nu}{1-\nu}\left(\frac{\Delta \delta_i}{\delta}\right)^2\right]\right\} \tag{13}$$

where the subscript i represents the defect type, and M,

δ, f_i, γ, and ν represent the average mass ($\Delta M_i = M - M_i$), ionic radius at position i ($\Delta\delta_i = \delta - \delta_i$), defect concentration, Grüneisen parameter, and Poisson ratio, respectively. Thus, the actual thermal conductivity was inversely proportional to f_i.

The thermal-expansion rates (Fig. 8(g)) indicate that the slopes of the curves were kept constant, indicating no phase transition with increased T. The CTEs of $5RE_2Zr_2O_7$, as shown in Fig. 8(h), ranged from 11.0×10^{-6} to 11.4×10^{-6} K^{-1} (within the temperature range of 573–1473 K), which were close to that of YSZ and larger than those of other samples, indicating its appropriateness to be used as TBCs. The relationship between the CTEs and thermal conductivities of the as-prepared $5RE_2Zr_2O_7$ and other works is listed in Fig. 8(i). Compared with YSZ and other TBCs such as $RE_2Si_2O_7$ [51], $RE_2Zr_2O_7$ [24], $RE_2Sn_2O_7$ [52], $REPO_4$ [11], and $RETaO_4$ [53], the as-prepared $5RE_2Zr_2O_7$ in this work had lower thermal conductivity and higher CTE, which is listed in Fig. 8(i), demonstrating the bright application prospects in the field of next-generation TBCs.

3. 3 Mechanical properties

E and HV (measured by Vickers indentation method) are shown in Fig. 9(a). We found that $5RE_2Zr_2O_7$ had improved E (262 GPa) and HV (11.78 GPa) compared with its counterparts. According to the previous work, E is positively correlated with the crystal cohesive energy (U), which can be expressed as Eq. (14) [53]:

$$U = \frac{N_A A z^+ z^- e^2}{R_0}\left(1 - \frac{1}{B}\right) \tag{14}$$

where N_A, A, z, e, R_0, and B represent the Avogadro's constant, Madelung constant, ionic charge, electron charge, balanced interionic distance, and Born exponent, respectively. Apparently, the U value has an inversely proportional relationship with R_0. The effective RE^{3+} ionic radius decreases with increased added number of RE elements (higher atomic number), leading to a shortened R_0. Therefore, the U value increases with the decreased R_0 value, resulting in an enhanced E [55]. The relationship between E and HV can be expressed as $E = 63.2 + 9.3HV$, indicating that E and HV present a directly proportional relationship [56]. Overall, the above analysis strongly proved that $5RE_2Zr_2O_7$ had higher E and HV than its counterparts. Figure 9(b) depicts K_{IC} calculated based on HV and E (the C value is shown in Fig. 9(c)). Notably, the K_{IC} of $5RE_2Zr_2O_7$ was as high as 2.7 $MPa \cdot m^{1/2}$, higher than that of YSZ (2.5 $MPa \cdot m^{1/2}$) [57] and nearly twice that reported for $La_2Zr_2O_7$ [2].

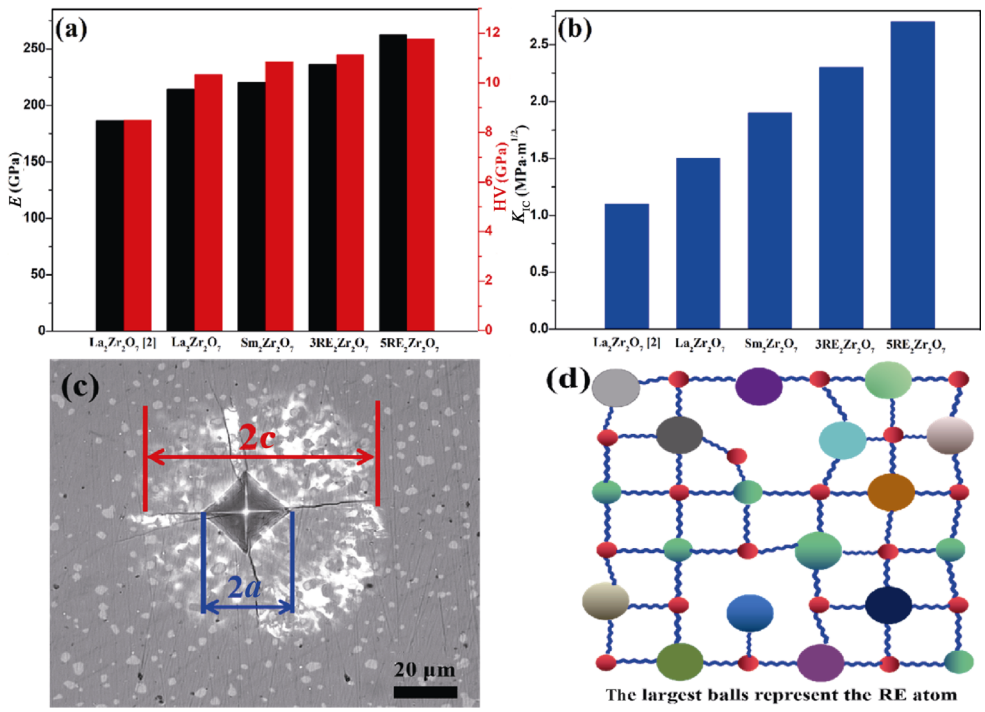

Fig. 9 (a) E and HV and (b) K_{IC} of the samples. (c) Typical photograph of the nano-indentation morphology of $5RE_2Zr_2O_7$ ceramics under a 100 g indentation load. (d) Schematic of the lattice framework of $5RE_2Zr_2O_7$.

The schematic of the lattice framework of $5RE_2Zr_2O_7$ (Fig. 9(d)) presents randomly occupied RE cations and different sizes between Zr and RE. This kind of outstanding disordered composition configuration demonstrated the cocktail effect, including mass difference, chemical bonding deviation, and local lattice distortion, which together affected the mechanical properties of the samples. Furthermore, a good damage tolerance of the ceramics can be characterized through the brittleness index (M) [58]:

$$M = \frac{\mathrm{HV}}{K_{\mathrm{IC}}} \tag{15}$$

Accordingly, the M value of the samples was calculated to be 4.36 $\mu m^{-1/2}$, lower than that reported for YSZ (7 $\mu m^{-1/2}$) [59], indicating that the as-prepared $5RE_2Zr_2O_7$ had better damage tolerance.

4 Conclusions

A new advanced high-speed positive grinding strategy combined with solid-state reaction method was used to successfully fabricate and systematically investigate $5RE_2Zr_2O_7$ HE-REZs. The results indicated that the samples formed a homogeneous single defective fluorite-type structure without any elemental segregation. ΔG_{mix} calculated through the first-principles calculations showed the feasibility to form $5RE_2Zr_2O_7$ HE-REZs in the thermodynamic direction. The as-prepared $5RE_2Zr_2O_7$ HE-REZs also exhibited good high-temperature phase stability and excellent thermophysical properties (low thermal conductivity and high CTEs). The $5RE_2Zr_2O_7$ HE-REZs also had ideal mechanical properties (E and K_{IC}) owing to their high U. The excellent integrated properties of the as-prepared $5RE_2Zr_2O_7$ HE-REZs demonstrated their potential as a new type of next-generation TBCs.

Acknowledgements

This work is supported by the National Science and Technology Major Project (2017-VI-0020-0093) and the National Natural Science Foundation of China (12090031). By the way, the authors would like to thank Jinghua XU from Shiyanjia Lab (www.shiyanjia.com) for the TG/DSC analysis. The authors would like to thank the Analysis and Testing Center of Beijing Institute of Technology.

Declaration of competing interest

The authors have no competing interests to declare that are relevant to the content of this article.

References

[1] Vassen R, Cao XQ, Tietz F, *et al*. Zirconates as new materials for thermal barrier coatings. *J Am Ceram Soc* 2000, **83**: 2023–2028.

[2] Wu J, Wei XZ, Padture NP, *et al*. Low-thermal-conductivity rare-earth zirconates for potential thermal-barrier-coating applications. *J Am Ceram Soc* 2002, **85**: 3031–3035.

[3] Zhao ZF, Chen H, Xiang HM, *et al*. High entropy defective fluorite structured rare-earth niobates and tantalates for thermal barrier applications. *J Adv Ceram* 2020, **9**: 303–311.

[4] Padture NP, Gell M, Jordan EH. Thermal barrier coatings for gas-turbine engine applications. *Science* 2002, **296**: 280–284.

[5] Clarke DR, Phillpot SR. Thermal barrier coating materials. *Mater Today* 2005, **8**: 22–29.

[6] Vaßen R, Jarligo MO, Steinke T, *et al*. Overview on advanced thermal barrier coatings. *Surf Coat Technol* 2010, **205**: 938–942.

[7] Liu B, Liu YC, Zhu CH, *et al*. Advances on strategies for searching for next generation thermal barrier coating materials. *J Mater Sci Technol* 2019, **35**: 833–851.

[8] Clarke DR, Oechsner M, Padture NP. Thermal-barrier coatings for more efficient gas-turbine engines. *MRS Bull* 2012, **37**: 891–898.

[9] Zhou YC, Xiang HM, Feng ZH. Theoretical investigation on mechanical and thermal properties of a promising thermal barrier material: $Yb_3Al_5O_{12}$. *J Mater Sci Technol* 2014, **30**: 631–638.

[10] Curran JA, Kalkancı H, Magurova Y, *et al*. Mullite-rich plasma electrolytic oxide coatings for thermal barrier applications. *Surf Coat Technol* 2007, **201**: 8683–8687.

[11] Joulia A, Vardelle M, Rossignol S. Synthesis and thermal stability of $Re_2Zr_2O_7$ (Re = La, Gd) and $La_2(Zr_{1-x}Ce_x)_2O_{7-\delta}$ compounds under reducing and oxidant atmospheres for thermal barrier coatings. *J Eur Ceram Soc* 2013, **33**: 2633–2644.

[12] Du AB, Wan CL, Qu ZX, *et al*. Thermal conductivity of monazite-type $REPO_4$ (RE = La, Ce, Nd, Sm, Eu, Gd). *J Am Ceram Soc* 2009, **92**: 2687–2692.

[13] Ren K, Wang QK, Shao G, *et al*. Multicomponent high-entropy zirconates with comprehensive properties for advanced thermal barrier coating. *Scripta Mater* 2020, **178**: 382–386.

[14] Wright AJ, Wang QY, Ko ST, *et al*. Size disorder as a descriptor for predicting reduced thermal conductivity in medium- and high-entropy pyrochlore oxides. *Scripta Mater* 2020, **181**: 76–81.

[15] Subramanian MA, Aravamudan G, Subba Rao GV. Oxide pyrochlores—A review. *Prog Solid State Chem* 1983, **15**: 55–143.

[16] Strange P, Svane A, Temmerman WM, *et al*. Understanding the valency of rare earths from first-principles theory. *Nature* 1999, **399**: 756–758.

[17] Cao XQ, Vassen R, Tietz F, *et al*. New double-ceramic-layer thermal barrier coatings based on zirconia–rare earth composite oxides. *J Eur Ceram Soc* 2006, **26**: 247–251.

[18] Xu ZH, He LM, Mu RD, *et al*. Double-ceramic-layer thermal barrier coatings of $La_2Zr_2O_7$/YSZ deposited by electron beam-physical vapor deposition. *J Alloys Compd* 2009, **473**: 509–515.

[19] Cao XQ, Li JY, Zhong XH, *et al*. $La_2(Zr_{0.7}Ce_{0.3})_2O_7$—A new oxide ceramic material with high sintering-resistance. *Mater Lett* 2008, **62**: 2667–2669.

[20] Xiang HM, Xing Y, Dai FZ, *et al*. High-entropy ceramics: Present status, challenges, and a look forward. *J Adv Ceram* 2021, **10**: 385–441.

[21] Zhang RZ, Reece MJ. Review of high entropy ceramics: Design, synthesis, structure and properties. *J Mater Chem A* 2019, **7**: 22148–22162.

[22] Zhu JT, Meng XY, Xu J, *et al*. Ultra-low thermal conductivity and enhanced mechanical properties of high-entropy rare earth niobates (RE_3NbO_7, RE = Dy, Y, Ho, Er, Yb). *J Eur Ceram Soc* 2021, **41**: 1052–1057.

[23] Zhao ZF, Xiang HM, Dai FZ, *et al*. $(La_{0.2}Ce_{0.2}Nd_{0.2}Sm_{0.2}Eu_{0.2})_2Zr_2O_7$: A novel high-entropy ceramic with low thermal conductivity and sluggish grain growth rate. *J Mater Sci Technol* 2019, **35**: 2647–2651.

[24] Zhou L, Li F, Liu JX, *et al*. High-entropy thermal barrier coating of rare-earth zirconate: A case study on $(La_{0.2}Nd_{0.2}Sm_{0.2}Eu_{0.2}Gd_{0.2})_2Zr_2O_7$ prepared by atmospheric plasma spraying. *J Eur Ceram Soc* 2020, **40**: 5731–5739.

[25] Li F, Zhou L, Liu JX, *et al*. High-entropy pyrochlores with low thermal conductivity for thermal barrier coating materials. *J Adv Ceram* 2019, **8**: 576–582.

[26] Segall MD, Lindan PJD, Probert MJ, *et al*. First-principles simulation: Ideas, illustrations and the CASTEP code. *J Phys Condens Matter* 2002, **14**: 2717–2744.

[27] Perdew JP, Burke K, Ernzerhof M. Generalized gradient approximation made simple. *Phys Rev Lett* 1996, **77**: 3865–3868.

[28] Miracle DB, Senkov ON. A critical review of high entropy alloys and related concepts. *Acta Mater* 2017, **122**: 448–511.

[29] Wang J, Wu FS, Zou RA, *et al*. High-entropy ferroelastic rare-earth tantalite ceramic: $(Y_{0.2}Ce_{0.2}Sm_{0.2}Gd_{0.2}Dy_{0.2})TaO_4$. *J Am Ceram Soc* 2021, **104**: 5873–5882.

[30] Leitner J, Voňka P, Sedmidubský D, *et al*. Application of Neumann–Kopp rule for the estimation of heat capacity of mixed oxides. *Thermochimica Acta* 2010, **497**: 7–13.

[31] He JJ, He G, Liu J, *et al*. New class of high-entropy defect fluorite oxides $RE_2(Ce_{0.2}Zr_{0.2}Hf_{0.2}Sn_{0.2}Ti_{0.2})_2O_7$ (RE = Y, Ho, Er, or Yb) as promising thermal barrier coatings. *J Eur Ceram Soc* 2021, **41**: 6080–6086.

[32] Burggraaf AJ, van Dijk T, Verkerk MJ. Structure and conductivity of pyrochlore and fluorite type solid solutions. *Solid State Ionics* 1981, **5**: 519–522.

[33] Vayer F, Decorse C, Bérardan D, *et al*. New entropy-stabilized oxide with pyrochlore structure: $Dy_2(Ti_{0.2}Zr_{0.2}Hf_{0.2}Ge_{0.2}Sn_{0.2})_2O_7$. *J Alloys Compd* 2021, **883**: 160773.

[34] Liu Y, Withers RL, Norén L. The pyrochlore to 'defect fluorite' transition in the $Y_2(Zr_yTi_{1-y})_2O_7$ system and its underlying crystal chemistry. *J Solid State Chem* 2004, **177**: 4404–4412.

[35] Zhu JT, Meng XY, Zhang P, *et al*. Dual-phase rare-earth-zirconate high-entropy ceramics with glass-like thermal conductivity. *J Eur Ceram Soc* 2021, **41**: 2861–2869.

[36] Feng J, Xiao B, Wan CL, *et al*. Electronic structure, mechanical properties and thermal conductivity of $Ln_2Zr_2O_7$ (Ln = La, Pr, Nd, Sm, Eu and Gd) pyrochlore. *Acta Mater* 2011, **59**: 1742–1760.

[37] Teng Z, Zhu LN, Tan YQ, *et al*. Synthesis and structures of high-entropy pyrochlore oxides. *J Eur Ceram Soc* 2020, **40**: 1639–1643.

[38] Wan CL, Qu ZX, Du AB, *et al*. Order–disorder transition and unconventional thermal conductivities of the $(Sm_{1-x}Yb_x)_2Zr_2O_7$ series. *J Am Ceram Soc* 2011, **94**: 592–596.

[39] Glerup M, Nielsen OF, Poulsen FW. The structural transformation from the pyrochlore structure, $A_2B_2O_7$, to the fluorite structure, AO_2, studied by Raman spectroscopy and defect chemistry modeling. *J Solid State Chem* 2001, **160**: 25–32.

[40] Díaz M, Pecharromán C, del Monte F, *et al*. Synthesis, thermal evolution, and luminescence properties of yttrium disilicate host matrix. *Chem Mater* 2005, **17**: 1774–1782.

[41] Zhou L, Huang ZY, Qi JQ, *et al*. Thermal-driven fluorite–pyrochlore–fluorite phase transitions of $Gd_2Zr_2O_7$ ceramics probed in large range of sintering temperature. *Metall Mater Trans A* 2016, **47**: 623–630.

[42] Kong LG, Karatchevtseva I, Gregg DJ, *et al*. $Gd_2Zr_2O_7$ and $Nd_2Zr_2O_7$ pyrochlore prepared by aqueous chemical synthesis. *J Eur Ceram Soc* 2013, **33**: 3273–3285.

[43] Pan W, Phillpot SR, Wan CL, *et al*. Low thermal conductivity oxides. *MRS Bull* 2012, **37**: 917–922.

[44] Zhao M, Ren XR, Yang J, *et al*. Low thermal conductivity of rare-earth zirconate–stannate solid solutions $(Yb_2Zr_2O_7)_{1-x}(Ln_2Sn_2O_7)_x$ (Ln = Nd, Sm). *J Am Ceram Soc* 2016, **99**: 293–299.

[45] Sood A, Cheaito R, Bai TY, *et al*. Direct visualization of thermal conductivity suppression due to enhanced phonon scattering near individual grain boundaries. *Nano Lett* 2018, **18**: 3466–3472.

[46] Zhou FF, Wang Y, Cui ZY, *et al*. Thermal cycling behavior of nanostructured 8YSZ, SZ/8YSZ and 8CSZ/8YSZ thermal barrier coatings fabricated by atmospheric plasma spraying. *Ceram Int* 2017, **43**: 4102–4111.

[47] Sun ZQ, Li MS, Zhou YC. Thermal properties of single-phase Y_2SiO_5. *J Eur Ceram Soc* 2009, **29**: 551–557.

[48] Braun JL, Rost CM, Lim M, *et al*. Charge-induced disorder controls the thermal conductivity of entropy-stabilized oxides. *Adv Mater* 2018, **30**: 1805004.

[49] Callaway J, von Baeyer HC. Effect of point imperfections on lattice thermal conductivity. *Phys Rev* 1960, **120**: 1149–1154.

[50] Wan CL, Pan W, Xu Q, *et al*. Effect of point defects on the thermal transport properties of$(La_xGd_{1-x})_2Zr_2O_7$: Experiment and theoretical model. *Phys Rev B* 2006, **74**: 144109.

[51] Tian ZL, Zheng LY, Li ZJ, *et al*. Exploration of the low thermal conductivities of γ-$Y_2Si_2O_7$, β-$Y_2Si_2O_7$, β-$Yb_2Si_2O_7$, and β-$Lu_2Si_2O_7$ as novel environmental barrier coating candidates. *J Eur Ceram Soc* 2016, **36**: 2813–2823.

[52] Qu ZX, Wan CL, Pan W. Thermophysical properties of rare-earth stannates: Effect of pyrochlore structure. *Acta Mater* 2012, **60**: 2939–2949.

[53] Chen L, Hu MY, Wu P, *et al*. Thermal expansion performance and intrinsic lattice thermal conductivity of ferroelastic $RETaO_4$ ceramics. *J Am Ceram Soc* 2019, **102**: 4809–4821.

[54] Xu L, Wang HJ, Su L, *et al*. A new class of high-entropy fluorite oxides with tunable expansion coefficients, low thermal conductivity and exceptional sintering resistance. *J Eur Ceram Soc* 2021, **41**: 6670–6676.

[55] Yang KL, Chen L, Wu FS, *et al*. Thermophysical properties of $Yb(Ta_xNb_{1-x})O_4$ ceramics with different crystal structures. *Ceram Int* 2020, **46**: 28451–28458.

[56] Zong RF, Wu FS, Song P, *et al*. Influence of zirconia alloying on the thermophysical and mechanical properties of $YTaO_4$ ceramics. *Ceram Int* 2019, **45**: 24894–24899.

[57] Kibsey M, Romualdez J, Huang X, *et al*. Mechanical properties of titania-doped yttria stabilized zirconia (TiYSZ) for use as thermal barrier coating (TBC). *J Eng Gas Turbines Power* 2011, **133**: 122101.

[58] Boccaccini AR. Machinability and brittleness of glass-ceramics. *J Mater Process Technol* 1997, **65**: 302–304.

[59] NIST Material Properties Database in web of the American Ceramics Society. Available at https://www.nist.gov/srd/online-scientific-databases.